

# Wind tunnel testing of a Formula Student vehicle for checking CFD simulation trends

Proc IMechE Part D:  
J Automobile Engineering  
2024, Vol. 238(14) 4347–4363  
© IMechE 2023  
Article reuse guidelines:  
sagepub.com/journals-permissions  
DOI: 10.1177/09544070231203076  
journals.sagepub.com/home/pid



Jaime Pacheco<sup>1</sup>, André C Marta<sup>2</sup>  and Luis Eça<sup>1</sup>

## Abstract

The aerodynamic performance analysis of Formula Student racecars has been mostly done by teams with CFD tools, for time and cost savings, that often lack proper validation. To address this, the FST Lisboa team performed a detailed wind tunnel (WT) test campaign, using a one-third scale model, under different configurations, including variable ride heights, bullhorn appendix, and rear wing flap settings, also replicated in CFD. The simulations used RANS with the SST k- $\omega$  turbulence model, with a 13.7 million polyhedral mesh for the test chamber region domain. Both experimental and numerical errors were estimated from the instrumentation and mesh convergence analysis, respectively. Comparisons were made between WT and CFD both in terms of local flow, using tufts for flow visualization, and global flow, using lift, drag, and pitching moment coefficients. Overall, the numerical streamlines agreed very well with the orientations of the tufts in experiments, but some discrepancies were found in regions of cross-flow and high-frequency unsteadiness, mainly caused by limitations of the visualization technique. The gamma transition model in CFD was abandoned as it could not replicate the WT observations. In terms of aerodynamic coefficients, a strong correlation was found between WT and CFD. The parametric studies revealed that the simulations captured the experimental sensitivity to each car setting parameter studied but the uncertainties did not enable a full quantitative evaluation of the aerodynamic performance. The drag reduction system significantly impacted the aerodynamic balance of the racecar, while the current bullhorn design proved to be ineffective. The ride height increase led to higher downforce, mostly due to the higher pitch angle of the vehicle, with negligible variation of the aerodynamic balance. This work validated the team CFD studies, building confidence in that trends estimated in numerical parametric studies are likely to be translated to the real prototype performance.

## Keywords

Six-component force balance, flow visualization, experimental procedure, numerical errors, drag reduction system, ride height, bullhorn

Date received: 18 November 2022; accepted: 17 August 2023

## Introduction

The usage of aerodynamic appendices in motorsport was introduced in the late 1960s, when experimental tests were the only option to develop aerodynamic designs.<sup>1</sup> Since then, the advances in computational power, together with the development of numerical methods, led to the ever expanding field of computational fluid dynamics (CFD).<sup>2</sup> Despite substantial progresses, CFD simulations still cannot accurately capture the complex physics of the flow around a race car, in particular for drag estimation and vortices generation and interaction.<sup>3</sup> Consequently, both computational simulations and experimental tests are used concurrently in the design process of race cars as they complement each other.

Track testing is expensive, and often limited, making wind tunnel (WT) testing the preferred option to recreates on-track conditions in a controlled environment, capable of producing reliable data that can simultaneously also be used to assess CFD modeling quality. In motorsport, WT tests use reduced scale models not only

<sup>1</sup>Instituto Superior Técnico, Universidade de Lisboa, Lisboa, Portugal

<sup>2</sup>IDMEC, Instituto Superior Técnico, Universidade de Lisboa, Lisboa, Portugal

### Corresponding author:

André C Marta, Department of Mechanical Engineering, Instituto Superior Técnico, Universidade de Lisboa, Avenida Rovisco Pais, 1, Lisboa 1049-001, Portugal.

Email: andre.marta@tecnico.ulisboa.pt

to minimize costs and facilitate manufacturing but also to comply with restricted test cross-sections.<sup>4</sup>

In order to challenge college students and engage future automotive engineers in the design, manufacturing, and competition of single-seat formula race cars, the Formula SAE was created under the sponsorship of the Society of Automotive Engineers (SAE) and first run in 1981 in the USA. Since 1998, this competition format has also been run in Europe, under the name Formula Student (FS), with minor changes.<sup>5</sup> Currently, the prototypes are divided into three categories: Combustion (FSC), Electric (FSE), and Driverless (FSD).<sup>6</sup> Each competition is divided into static and dynamic events. The engineering process behind the car design is presented in three static events – Engineering Design, Business Plan, and Cost and Manufacturing, while the racetrack performance is demonstrated in six dynamic events – Acceleration, Skid Pad, Autocross, Endurance (Combustion and Electric) or Track Drive (Driverless), and Efficiency. Formula Student Técnico (FST) is the racing team from Instituto Superior Técnico (IST) that competes in both the Electric and Driverless categories.

In the last few years, aerodynamics took a fundamental share of the FS cars performance, with almost every team developing aerodynamic packages to improve balance and handling. The current aerodynamic design philosophy privileges downforce at the expense of additional drag, as most cars are overpowered, and the latest prototype FST10e was no exception, as illustrated in Figure 1. Its aerodynamic package is divided into four major sub-assemblies: (i) Front wing, generates downforce with a high efficiency and redirects the air to the other aerodynamic devices; (ii) Underbody, creates suction underneath the car by accelerating the airflow. A rear diffuser is used to enhance that acceleration; (iii) Side Elements, produce downforce and redirect the airflow; (iv) Rear Wing, generates high downforce but also high drag.

WT testing is a common practice in the car industry. However, it is seldom used by Formula Students teams because it requires access to costly and complex facilities. Consequently, teams often trust their CFD simulations without assessing the modeling accuracy of the results (validation). Nevertheless, in the last years, some teams are investing resources to build trustful correlations between WT testing, CFD simulations, and on-track testing.

A Formula Student race car is approximately 3 m long, 1.5 m wide, and 1.2 m high, limited by regulations<sup>6</sup> so scale models often have to be used. However, some FS teams have taken advantage of having access to large WT used by major car manufacturers that allow testing of real-size prototypes.

The ReenTeam Uni Stuttgart tested their race car in a wind tunnel equipped with a moving ground and front wheels rotation. Deviations of 3% regarding aerodynamic efficiency were obtained when compared to transient Detached Eddy Simulation (DES), increasing

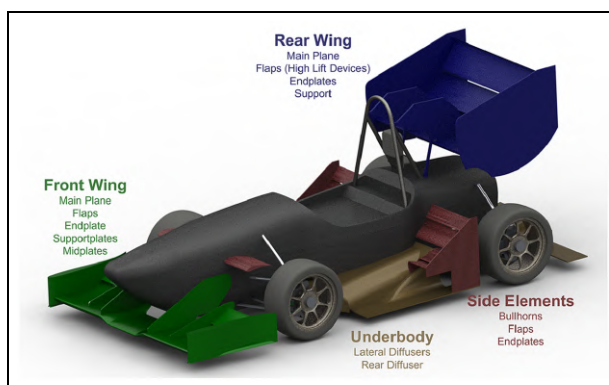


Figure 1. Aerodynamic concept of the FST10e prototype.

to 7% when compared to time-averaged DES simulations.<sup>7</sup> The data gathered was then compared against on-track testing. Overall, the CFD results and WT testing presented a high correlation with on-track testing.

The AMZ Racing team went even further with its efforts to validate the design decisions made through CFD simulations, partnering with developers of a measurement system that consisted of a hand-held probe. It records the instantaneous velocity field while the system keeps track of the probe position enabling the visualization of the flow field in real-time and map streamlines. Overall, CFD simulations matched the WT results despite some local inconsistencies.<sup>8</sup>

The Southampton University team pioneered the construction of a modular WT model with built-in actuators to evaluate the aerodynamic sensitivity across several configurations (roll, pitch, and front and rear ride heights) achieved during on-track testing.<sup>9</sup> Some tests were already performed but there are no results available yet.

Until recently, the FST team have developed some knowledge of wind tunnel testing. The first consisted of a 40% scale model of the FST06e rear wing. However, it was only possible to test at a Reynolds number 3.75 times lower than the design due to limitations in the maximum airflow speed, which led to very inconsistent results when compared to CFD. Later, a 25% scale model of the complete FST06e was 3D printed and tested. In this case, the reduced material thicknesses caused aeroelastic phenomena, so no clear findings were achieved.

In order to boost the FST car aerodynamic design capability, that have been mainly based on CFD, inconclusive WT tests and rare on-track tests with limited instrumentation, the present work intends to build a trustful correlation between WT testing and CFD simulations. It should provide not only an assessment of the quality of the numerical simulations used by the team but also become the basis for future routine WT testing. To that end, a complete one-third scale model of the newest prototype, the FST10e, was built and tested in a large WT facility at different operating conditions and configurations. However, this facility was

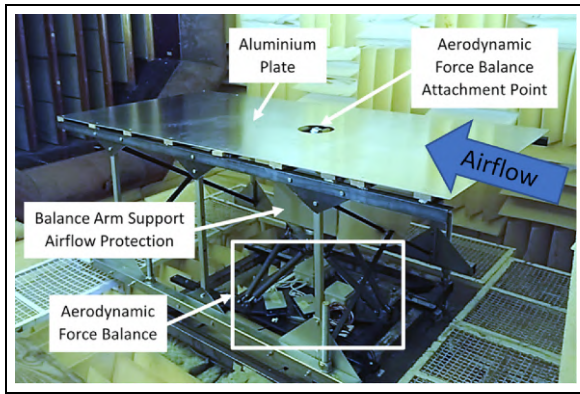


**Figure 2.** Wind tunnel facility with ground and force balance mounted.

upgraded to make the test of race cars possible, namely regarding the aerodynamic force balance and its support and also a plate to mimic the ground effect. The exact conditions will be modeled in CFD so that a direct comparison between numerical and experimental data can be performed.

This manuscript is divided in six main sections, following this introduction, namely: (i) WT Testing Facility, contains the description and characterization of the WT and its instrumentation; (ii) Mathematical Formulation, includes CFD setup, models, boundary conditions, mesh convergence, and numerical error assessment; (iii) Formula Student Model, describes the scale model, its manufacturing, and its positioning in the airflow; (iv) Experimental Setup, lists the car operating conditions and configurations tested and details the adopted procedure; (v) Flow Visualization, qualitatively evaluates the numerical simulation using wool tufts; (vi) Aerodynamic Loads, quantitatively compares the loads measured in WT with those estimated by CFD simulations. It concludes by summarizing the main achievements.

## Wind tunnel testing facility

### Wind tunnel

The experiments were performed in the closed return aeroacoustic wind tunnel with a open test section at Aerospace Engineering Laboratory at IST. The wind tunnel has a seven-blade fan powered by a 200 kW motor that produces an airflow speed up to 50 m/s. The inlet nozzle at the test chamber has 1.5 m diameter, with an upstream honeycomb grid that helps producing a low turbulence, uniform airflow.

Reproducing on-road operating conditions in WT can be quite difficult<sup>10</sup> because it implies handling the relative motion of the car on the ground, taking special care with the boundary layers that develop inside the WT test section. Among the several boundary layer control techniques available,<sup>11,12</sup> an elevated model with ground plate was selected as it implied the least

amount of modifications to the available WT facility. Since the wheels of the model did not include motion, a small gap with the plate was adopted to minimize the ground effect.<sup>13</sup> This approach also facilitated the measurement of the aerodynamic loads since the model was exclusively suspended on the force balance without interference.

Before this work, the WT facility was not prepared for testing a road car model. Thus, several steps upgrades were made: (i) a steel frame bolted onto concrete under the WT test chamber floor was constructed to provide robust, vibration-free, fixed support for the force balance; (ii) a steel, deformation-free, bed frame, with an aluminum table top 2 m long, 1 m wide, and 3 mm thick to mimic the ground, plate was built and fixed to the support. The resulting apparatus is shown in Figure 2.

### Airflow characterization

Velocity measurements were taken along several sections to identify the turbulence intensity, cross-section velocity profiles, and axial velocity evolution inside the test chamber using constant temperature anemometry. A low-inertia, thin metal wire, probe was used to get fast-response velocity measurements in the turbulent flow. The wire was first electrically heated to temperatures higher than the airflow, then the current variation required to maintain constant temperature when exposed to increasing airflow speed was measured with an electrical sensor, allowing to estimate the airflow speed.<sup>14</sup>

A differential pressure sensor *Schlumberge*<sup>®</sup> *H5010*, coupled with the *Schlumberger*<sup>®</sup> *D5484* signal conditioner with a Prandtl probe was first calibrated inside a room with a controlled environment. A direct current source *TTI TSX3510* powered the sensor and the output voltage was measured with a digital multimeter *HP 34401A*. The airflow speed was then calculated from the measured dynamic pressure using the Bernoulli's principle<sup>15</sup> for air properties at room conditions. This data allowed for not only for an accurate setting of the WT airflow speed but also to calibrate the anemometer. The constant temperature hot film anemometer used was the *TSI Incorporated*<sup>®</sup> *Model 1750*. It was calibrated using 17 calibrations points that uniformly span the speed range from 0 to 45 m/s. The anemometry data was recorded with a 16-bit *National Instruments*<sup>™</sup> *NI PCIe – 6321* acquisition system.

The airspeed measurements were taken at a nominal freestream airspeed  $u_0 = 25$  m/s, maintaining a stable temperature around 27°C, at five cross-sections located at  $x = 315, 415, 515, 1030,$  and 2330 mm from the WT nozzle exit. The first three sections were between the nozzle and the predicted testing location of the car model, the fourth was at the middle of that location and the fifth was behind. During the anemometry, 35 data points separated by 2 mm radially from the centerline of the jet section were extracted for each section.

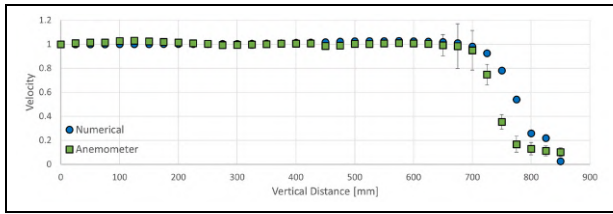


Figure 3. Wind tunnel velocity profile at  $x = 315$  mm.

The resulting data was used to define the boundary conditions of the numerical simulations and present an initial comparison between the experimental and numerical simulations. The CFD simulations were performed without any model to reproduced the wind tunnel measurements.

Figure 3 presents the velocity profile of the airflow at  $x = 315$  mm. The uniform flow is reached between  $z = 0$  (jet center) and  $z = 675$ , from where the shear layers are noticeable as the velocity gradient increases heavily.

In turn, Figure 4 shows the evolution of the normalized velocity along the streamwise ( $x$ -axis) direction of the WT test section, at four radial locations:  $z = 0$  (jet center), 250, 500, and 750 mm (exit nozzle radius). Along the first three inner most radial locations ( $z = 0, 250$  and  $500$  mm), the airflow speed remains almost constant streamwise, which means the flow in the center of the test section holds its freestream unperturbed nature. Here, the CFD data presents a very satisfactory correlation with the experimental data. In contrast, at the outer radial location corresponding to the nozzle radius ( $z = 750$  mm), the velocity decreases near the nozzle exit, followed by a notorious increase downstream. The experimental data exhibits a larger increase than CFD, which can be justified by the higher turbulence intensity felt around this radial location, where the free jet mixing boundary layer develops.

To quantify the turbulence intensity of the WT, a statistical analysis was made of the measured velocity fluctuations.<sup>16</sup>

The velocity field  $u(t)$  was decomposed in two components: the mean value,

$$\bar{u}(t) \equiv \bar{u} = \lim_{t \rightarrow \infty} \frac{1}{t} \int_{t_0}^{t_0+t} u(t) dt \equiv \frac{1}{N} \sum_1^N u \quad (1a)$$

defined by a simple mean value method since the velocities in study are supposed to be constant in time, and the fluctuations,

$$u'(t) = u(t) - \bar{u}, \quad (1b)$$

The root mean square of fluctuations is,

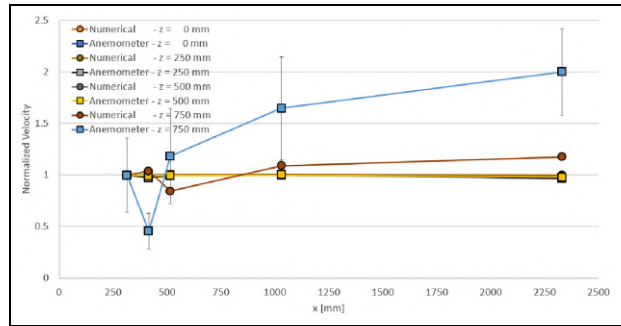


Figure 4. Wind tunnel velocity streamwise evolution.

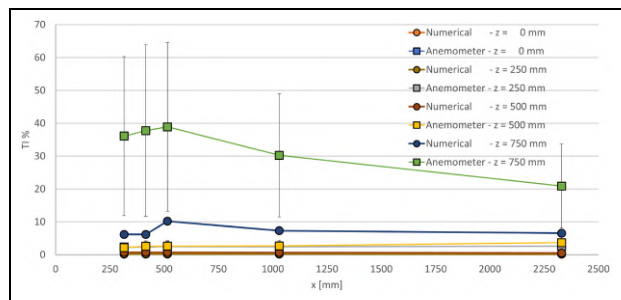


Figure 5. Wind tunnel turbulence intensity streamwise evolution.

$$u'_{rms} = \sqrt{\frac{1}{N} \sum_1^N (u - \bar{u})^2}. \quad (1c)$$

Consequently, the turbulence intensity was then estimated as

$$TI = \frac{u'_{rms}}{\bar{u}}, \quad (2)$$

assuming an axisymmetric jet and isotropic turbulence ( $u'_x = u'_y = u'_z$ ). The turbulence intensity evolution along the streamwise is presented in Figure 5 at the same radial locations. The turbulence intensity behavior was qualitatively compared between the experiments and the CFD simulations to assess the quality of the latter, keeping in mind that the turbulence intensity was imposed at the CFD domain inlet boundary (see Figure 8). Overall, the numerical data presents the same trend as the experimental data. On one hand, regarding the inner radial locations  $z = 0, 50$  and  $500$  mm, the experimentally measured turbulence intensity increases gradually with the distance to the nozzle as the shear layers grow, but the mean value remains approximately at 2%. In contrast, the numerical simulations predicted a turbulence intensity of 0.25%, which is highly dependent on the inlet boundary condition. Even if it were possible to measure the turbulence intensity at the

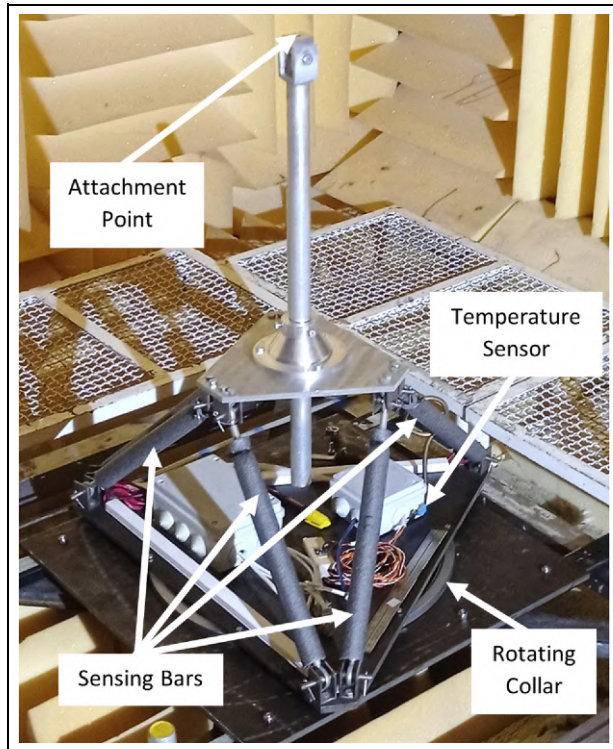


**Figure 6.** Aerodynamic force balance.

domain inlet, the CFD fails to accurately estimate its evolution as the domain inlet boundary conditions are defined far upstream from the test chamber, allowing a strong decay of the inflow quantities.<sup>17</sup> On the other hand, regarding the radial location entirely inside the free jet mixing shear layer ( $z = 750\text{mm}$ ), there is an expected increase in the turbulence intensity closer to the inlet due to the concentration of the turbulent energy of the large eddies. It later decays streamwise by the action of turbulence dissipation mechanisms.

### Aerodynamic force balance

To measure the loads acting on the model during testing, the WT was instrumented with the external, six-component, force balance shown in Figure 6, which had been designed, manufactured, and instrumented in-house by Oliveira.<sup>18</sup> Being an external balance, thus located outside the model, offers greater versatility for testing distinct models without significant modifications. Having six components, allows the recording of the 3D components of force (drag  $-F_x$ , side force  $F_y$ , and downforce  $-F_z$ ) and moment (roll  $M_x$ , pitch  $M_y$ , and yaw  $M_z$ ), as illustrated in Figure 9, which are essential to characterize the aerodynamic race car performance.

During data acquisition, some best practices<sup>14</sup> were followed: no balance interference with the airflow; model attachment remained untouched; forces applied on the vehicle carried exclusively to the load sensors and hysteresis controlled with pre-loads. Additional care included correcting the measured loads due to

model weight and off-setting vehicle attitude changes due to elastic deformation of the balance.<sup>19</sup> To account for the flow unsteadiness produced by vortex generation and periodic shedding, the data was sampled during a large time interval to calculate accurate time-averaged values.

A careful calibration process was followed to ensure the accurate measurement of the aerodynamic loads. The strain of each of the six sensing bars are registered using strain gauges coupled to two *National Instruments NI™9237* acquisition systems. Each sensing bar had a previously well identified transfer function from strain to axial force.<sup>18</sup> The calibration correlates the six outputs ( $F_x, F_y, F_z, M_x, M_y$ , and  $M_z$ ) with the axial force carried by each sensing bar. Different known loads were applied to the balance using a custom made apparatus that included pulleys and braces to allow for pure forces, pure moments, combined forces, and combined forces and moments. Since the CFD model of the WT experiment was already setup, it was possible to estimate the expected loads during the WT model testing. This way, the calibration load cases were planned such that the calibration matrix presented a higher data density near the expected loads.

The calibration methodology adopted was the following: initially all supports were pre-loaded with weights, then additional weights were added every 30 s. To allow for the complete damping of vibrations caused by loading process, only 15 s were used to calculate the average strain. Each load case sequence was repeated three times and a total of 267 load cases were tested. The postprocessing required to obtain the calibration coefficient matrices followed that described in Oliveira.<sup>18</sup> The obtained correlation was added to the balance user-interface in LabView™, which then presented and recorded the aerodynamic loads in their final form.

Before testing the model, the calibration was validated by loading the balance with new known load cases, focused on the main expected forces and moments (negative  $F_x$  for drag, negative  $F_z$  for downforce, and pitching moment  $M_y$ ). Unexpected dependency between these two forces were found for high loads so 36 new load cases were added to the calibration matrix to fix that. Nevertheless,  $F_x$  still presented a maximum variation around 6.9% when  $F_z$  is varying, as seen in the red circles in Figure 7(a), while looking at the inverse loading process in Figure 7(b) a maximum variation of only 1.7% is present in  $F_z$  when the maximum  $F_x$  load is applied.

## Mathematical formulation

### Numerical domain

To correlate the wind tunnel results with the CFD models, the numerical domain was the recreation of the aeroacoustic WT, where the experimental work took place. Only the part of the WT in the vicinity of the test chamber was modeled, with the numerical domain

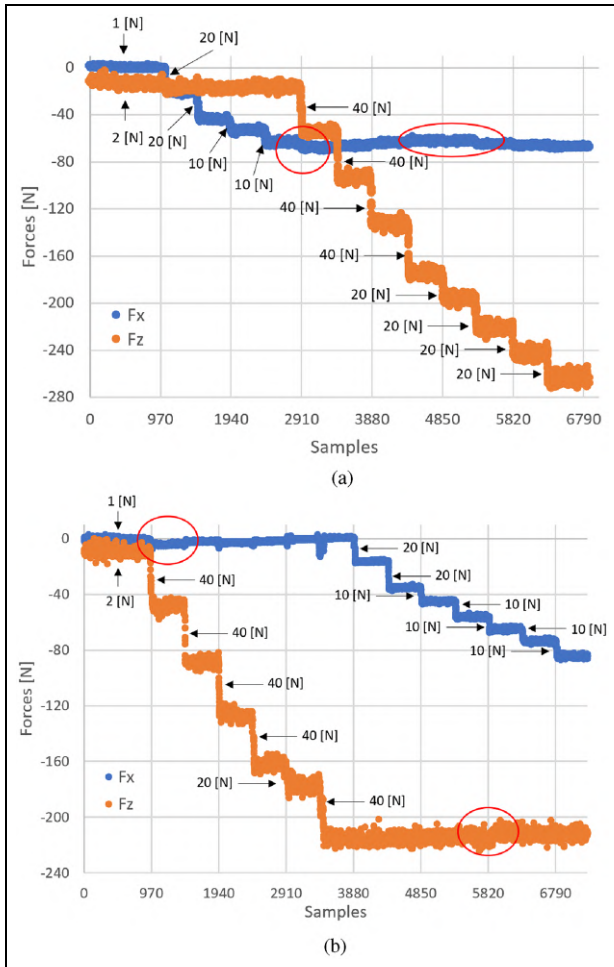
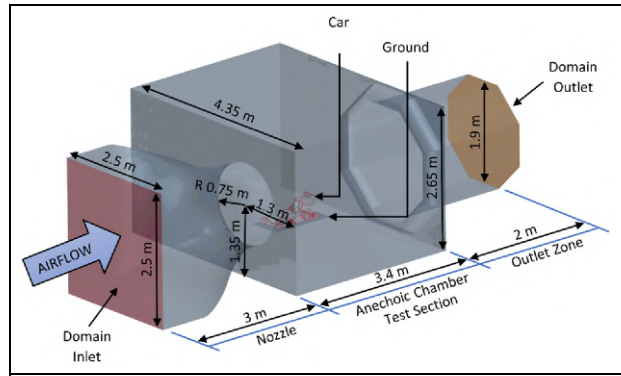


**Figure 7.** Force balance stabilization test cases  $F_x$  and  $F_z$ : (a)  $F_{x-}$  load until  $-61$  N followed by  $F_{z-}$  load and (b)  $F_{z-}$  load until  $-221$  N followed by  $F_{x-}$  load.

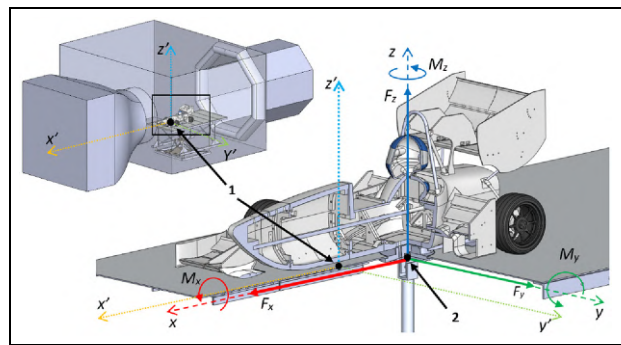
divided into three different zones – nozzle, test chamber, and outlet –, as presented in Figure 8 with general dimensions. The domain inlet matched the flow straightener location, which consisted of a fine honeycomb grid. The domain outlet is located at a distance that was found in studies to exhibit no significant difference in the flow around the vehicle if further increased.

Figure 9 shows the two coordinate systems used, one attached to the center of the front axle (1) to define the model location, and another attached to the balance support arm to easily compare the aerodynamic forces with the experiments, where the forces  $F = (F_x, F_y, F_z)$  and moments  $M = (M_x, M_y, M_z)$  relate to downforce  $L = -F_z$  and drag  $D = -F_x$ . In this study, only straight line conditions configurations were tested so the focus was on the components  $F_x$ ,  $F_z$ , and  $M_y$ . The downforce  $L$ , drag  $D$ , and pitching moment  $M_y$  loads are expressed in terms of their respective nondimensional coefficients,

$$C_L = \frac{L}{\frac{1}{2}\rho u_0^2 S}, \quad C_D = \frac{D}{\frac{1}{2}\rho u_0^2 S}, \quad C_M = \frac{M_y}{\frac{1}{2}\rho u_0^2 S b}, \quad (3)$$



**Figure 8.** Wind tunnel numerical domain.



**Figure 9.** Coordinate systems.

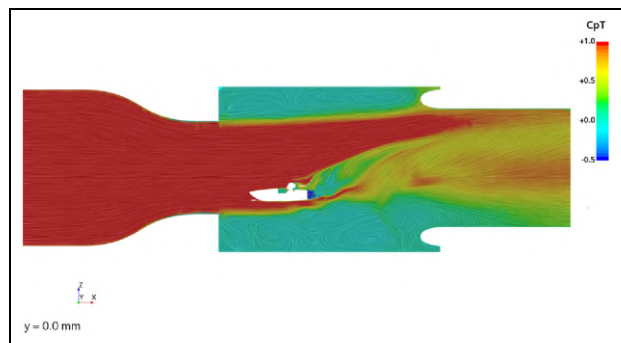


**Figure 10.** Total pressure coefficient at the center section ( $y=0$ ).

where  $u_0$  is the freestream air speed,  $\rho$  is the air density,  $S$  is the reference area, and  $b$  the reference length. In this work, the pitching moment was calculated about the model-balance attachment point. The FST10e frontal area ( $S \approx 1\text{m}^2$ ) and length ( $b \approx 3\text{m}$ ) were used as reference, scaled appropriately for the model as  $S_{model} = S \times scale^2$  and  $b_{model} = b \times scale$ , where  $scale = 1/3$ .

Sensitivity studies were performed to choose the suitable domain outlet location and the ground plate dimension, depending on their effect on the computed aerodynamic forces. These yield an outlet region extension of just 2 m, as displayed in Figure 10, where the

**Table 1.** Numerical downforce and drag coefficients for different ground plate dimensions.

Dim.	1.4×0.6m	2×1m	2.35×1.1m
$C_L$	3.153 (-4.86%)	3.314	3.327 (+0.41%)
$C_D$	1.494 (-4.01%)	1.556	1.558 (+0.11%)

total pressure coefficient at the center section ( $y = 0$ ) is shown. Despite the car model being around 1 m long and 0.5 m wide, the ground plate had to be substantially larger, resulting in a 2 m long by 1 m wide plate, as demonstrated in Table 1. These were the dimensions of the aluminum ground plate adopted for the experiments.

**Mathematical models**

The airflow expected while testing the car model is characterized by a Reynolds number  $Re > 10^6$ , with many small flow structures caused by the body geometry, thus predominantly turbulent.

The Reynolds-Average Navier–Stokes (RANS) equations with the SST  $k - \omega$  turbulence model were used for being the most appropriated to solve wall bounded flows and present great performance for complex boundary layer flows under adverse pressure gradients.<sup>20,21</sup> By switching between the  $k - \epsilon$  model in the freestream while resolving the near wall with the  $k - \omega$  model, the SST model is capable of accurately estimating not only the pressure drag as the  $k - \epsilon$  turbulence model, but also the viscous drag, which is equally important in the present work. This makes it the most commonly used eddy viscosity turbulence model in the motorsport industry.<sup>22</sup> Legacy CFD simulations conducted by the FST team supported this choice. Anticipating the occurrence of transition from laminar incoming flow to turbulent flow in the boundary layers over the car model, the  $\gamma$  transition model, a simplification of the  $\gamma - Re_\theta$  model that only solves the transport equation for intermittency but not for the momentum thickness Reynolds number, was coupled with the SST  $k - \omega$  turbulence model.<sup>23</sup>

StarCCM +<sup>®</sup> software was used to perform the CFD simulations. Regarding the boundary conditions, a uniform axial velocity was set at the domain inlet and an ambient static pressure prescribed at the outlet with velocity extrapolated from domain. The turbulence intensity was set to  $TI = 1\%$  and the turbulence viscosity ratio to  $\mu_T/\mu = 10$ . No-slip condition was set at all solid walls (car model, ground and wind tunnel). Air at standard sea-level conditions was assumed, with density  $\rho = 1.225\text{kg/m}^3$  and viscosity  $\mu = 1.8 \times 10^{-5} \text{ Pa}\cdot\text{s}$ .

The impact of the transition model was studied, with focus on the front wing, as it is one of the few car parts that might exhibit significant regions of laminar boundary-layers. Table 2 summarizes the downforce and drag coefficients evaluated with and without the  $\gamma$  transition

**Table 2.** CFD transition model impact study.

Transition model	None	$\gamma$ transition
Car total $C_L$	3.27	3.31
Car total $C_D$	1.55	1.56
Front wing $C_L$	0.98	1.01
Front wing $C_D$	0.14	0.14

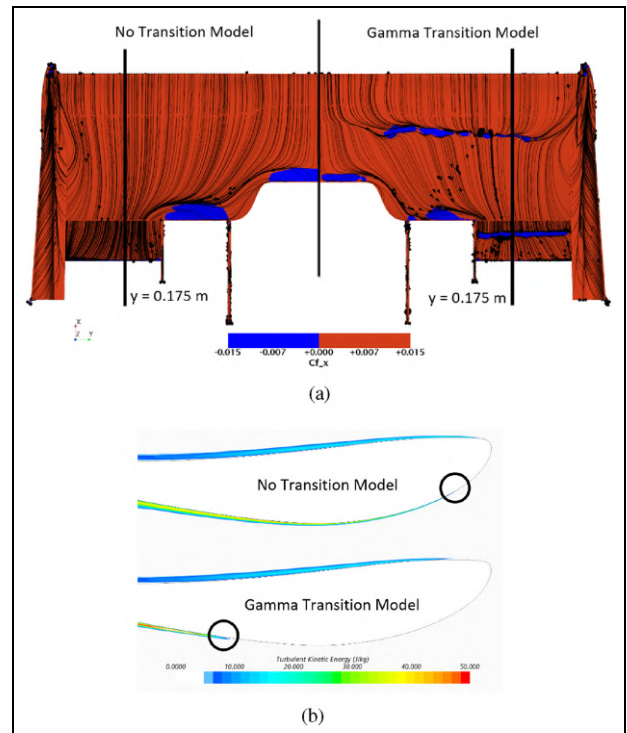


**Figure 11.** Front wing CFD results using different transition models: (a) skin friction coefficient and (b) turbulent kinetic energy.

model for a medium refinement level mesh. The differences regarding the force coefficients are almost negligible, even though there is a significant impact on the transition location as seen from the front wing suction side surface skin friction coefficient  $C_f$  in Figure 11(a). Transition was estimated to occur immediately after the leading edge of the main plane if no transition model is used, but moved downstream, caused by laminar separation bubbles under an adverse pressure gradient, when the  $\gamma$  model was used. The turbulent kinetic energy increase shown in Figure 11(b) along the section  $y = 0.175 \text{ m}$  corroborates the transition location.

**Mesh convergence**

The FST10e car was modeled in Solidworks<sup>®</sup> and then imported into StarCCM +<sup>®</sup>. Due to its complex geometry, the *surface wrapper* feature had to be applied after import to produce a clean geometry.

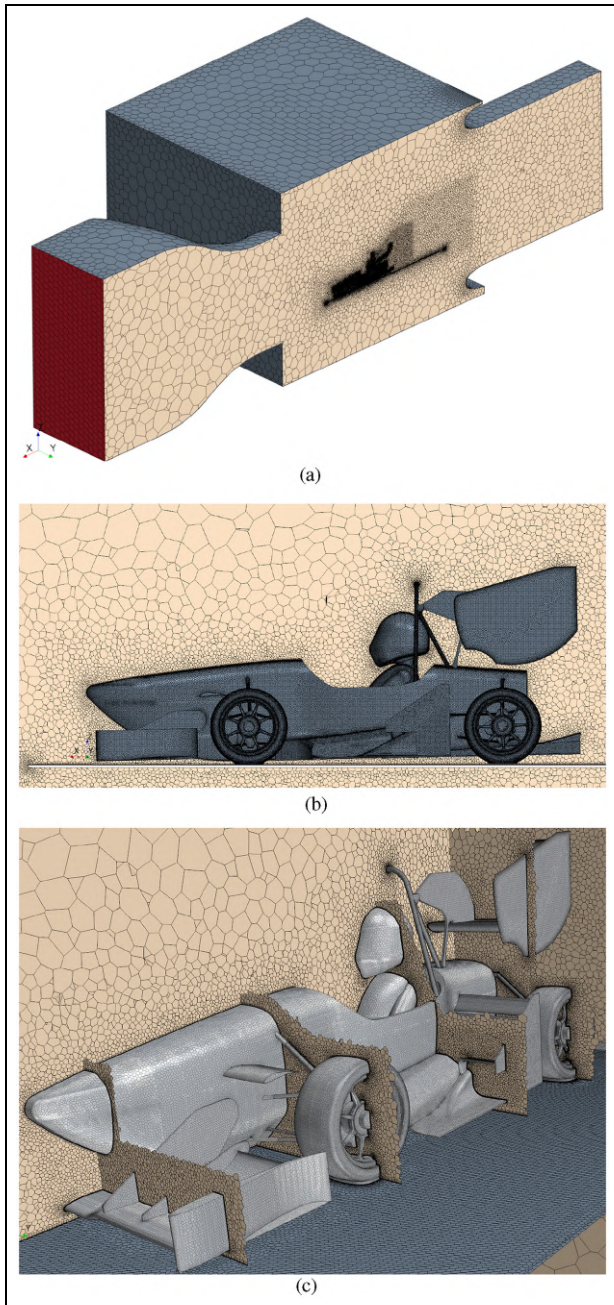


**Figure 12.** Hybrid polyhedral and prism layer mesh: (a) domain (sectioned), (b) vehicle (side view and midplane), and (c) vehicle (transverse planes).

A hybrid polyhedral and prism layer mesh was used to discretize the numerical domain, as seen in Figure 12. Polyhedral cells are constructed from tetrahedral cells that successfully adapt to the complex surface geometries, particularly where high refinement is required.<sup>24</sup> The prism layers are used on every solid wall, targeting a wall  $y^+ \leq 5$  to ensure that the first mesh node is inside the viscous sublayer, thus enabling the low  $y^+$  wall treatment.<sup>25</sup> This ensures high resolution to accurately predict transition and separation phenomena in the boundary layer, on which aerodynamic forces are highly dependent. The mesh adaptation included the use of

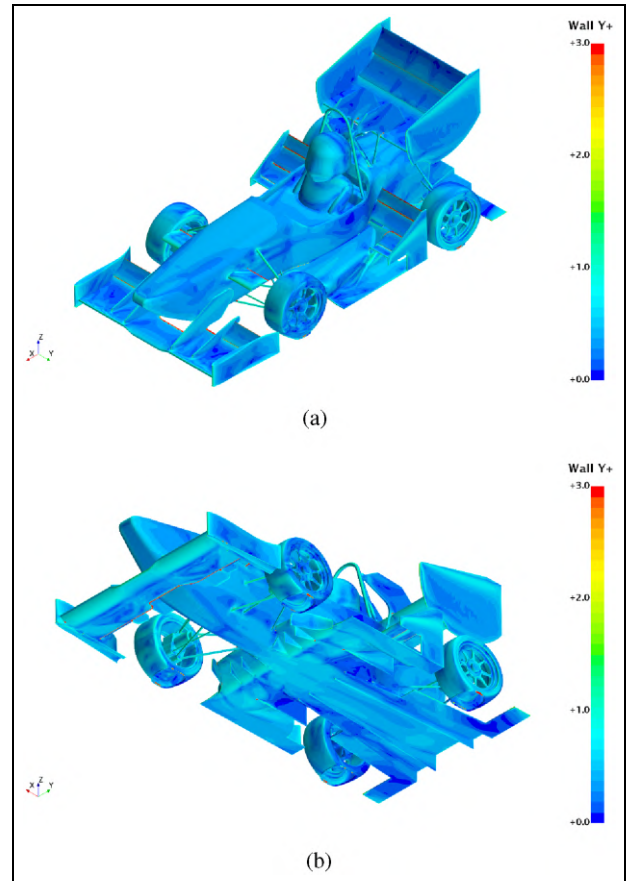


**Figure 13.** Wall  $y^+$  of medium refinement mesh: (a) top view and (b) bottom view.

volume controls to refine zones of the model where strong adverse pressure gradients and high vorticity were expected to capture the relevant small scales that affect the airflow. The resulting wall  $y^+$  on the car model surface is seen in Figure 13 for the medium refinement level mesh.

When numerically solving non-linear differential RANS equations, three type of errors arise: round-off, iterative, and discretization.<sup>26–28</sup> The round-off errors were kept at a minimum by performing the calculations with double-precision. The iterative errors were controlled by evaluating the stability and convergence of not only the residuals of the governing equations, with all non-normalized residuals dropping below  $10^{-3}$ , but also the computed aerodynamic loads. The discretization errors, dominant in complex geometries and high curvature surfaces<sup>26,29</sup> such as the car model, were estimated using a least-squares error estimation method. This method requires a mesh convergence study with at least three geometrically similar grids, being the discretization error  $e(\phi_i)$  estimated as<sup>30</sup>

$$e(\phi_i) = \phi_i - \phi_{exact} = \alpha h_i^p, \quad (4)$$

where  $\phi_{exact}$  is the estimate of the exact solution,  $\alpha$  is the error constant,  $p$  is the order of grid convergence,



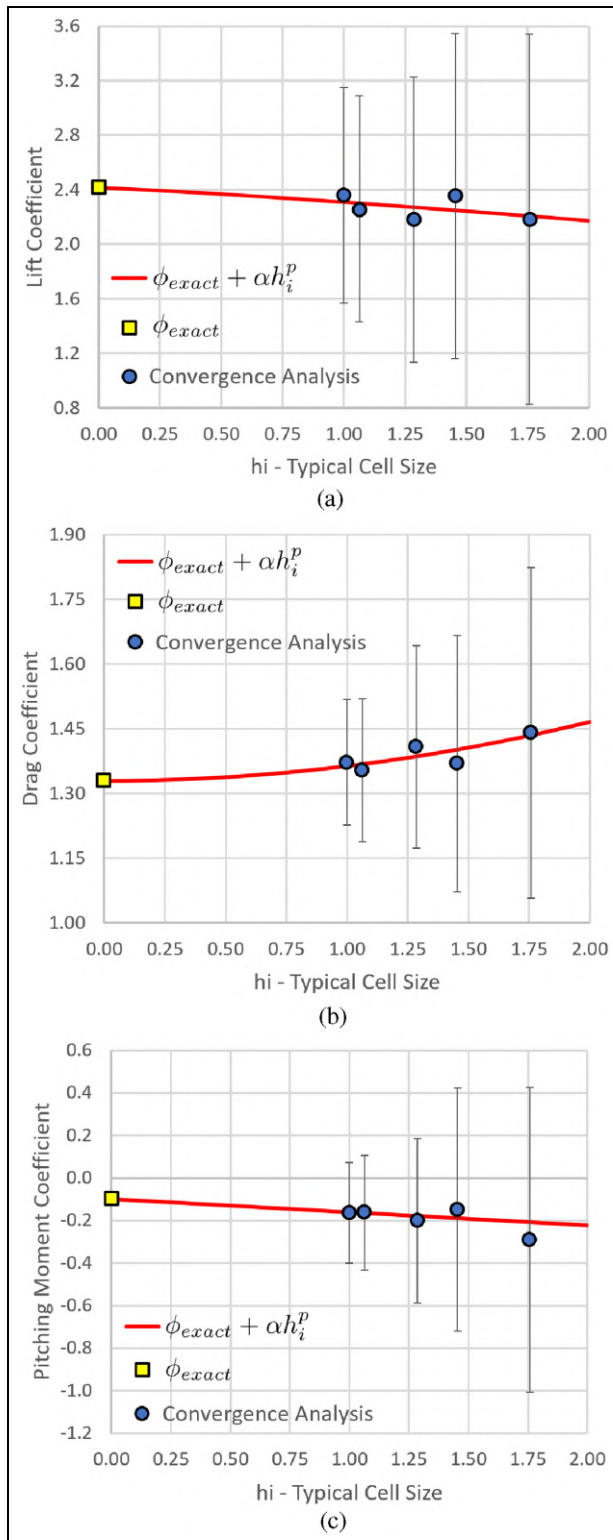


**Figure 14.** Numerical error uncertainties: (a) downforce coefficient, (b) drag coefficient, and (c) pitching moment coefficient.

and  $h_i$  is the typical cell size (that defines the refinement ratio  $r_i = h_i/h_1$ ), defined by  $h_i = \sqrt[3]{\frac{N_1}{N_i}}$ , where  $N_i$  is the number of elements of mesh  $i$  and  $N_1$  is the number of elements of the finest mesh. Five refinement levels were used in the grid convergence study to estimate the exact

value of downforce, drag, and pitching moment,  $C_L = -2.414$ ,  $C_D = 1.329$ , and  $C_M = -0.098$ , respectively, as seen in Figure 14. The medium refinement (mesh 3) was used for the remaining work as it represented a good compromise between numerical accuracy and simulation time. The estimated error of this 13.7 million cell mesh for the downforce ( $C_L$ ) and drag ( $C_D$ ) coefficients were 5.8% and 4.3%, respectively, and the total solver time was 17.5 h per simulation.

## Formula Student model

The wind tunnel test model was the FST10e, FST latest prototype, with external systems that did not have a significant impact on the car aerodynamics eliminated, such as the cooling system and electrical wires. Other components suffered small changes, such as: closing the cockpit, smoothing the sharp edges, and increasing the thickness of flaps trailing edges to ease manufacturing. The WT model weighed 9.35 kg and it was composed of 149 parts, excluding fixation elements.

Both, the real full size vehicle and the simplified CAD rendering of the wind tunnel model are shown in Figure 15(a) and (b), respectively. In turn, Figure 15(c) presents an overview of the general components used to assemble the FST10e model.

Two major manufacturing processes were used: 3D printing and Computerized Numerical Control (CNC) machining. The latter was used to cut the plywood flat components and the rear wing aluminum supports, while all the other components were 3D printed in Polylactic Acid (PLA). The *Ultimaker Cura*<sup>TM</sup> v.4.8.0 open source software was used to prepare the geometries to be printed by *Ultimaker 2 +*<sup>TM</sup>, *Ultimaker 2 + Extended*<sup>TM</sup>, and *Ultimaker 3*<sup>TM</sup> 3D printers at the *Laboratory of Biomechanics of Tissues and Biomaterials* in IST. The CNC design files were processed by *InoCONTROL*<sup>®</sup> to setup the CNC machine at the *iStart* laboratory in IST.

To recreate the conditions of road testing, the dimensionless Reynolds number was preserved, representing the ratio between inertial and viscous forces,  $Re = \frac{\rho V b}{\mu}$ , where  $V$  defines the airflow speed,  $b$  is the reference length, and  $\mu$  is the fluid dynamic viscosity.

A one-third scale was selected such that the model would completely lie inside the potential core of the WT airflow in the test chamber, previously carefully characterized with anemometry and confirmed with CFD that it remained so after placing the model in the test chamber. Given that the air density and viscosity is approximately the same for on-road and WT testing and that the FST10e average speed in competition is approximately 15 m/s, then the WT airspeed, which must scale with the inverse of the characteristic length,  $\frac{V_{model}}{V_{car}} = \frac{l_{car}}{l_{model}}$  had to be around 45 m/s to assure Reynolds similarity. Later it was found necessary to limit the WT airspeed to 25 m/s so that the air temperature inside it could be kept constant. This led to a

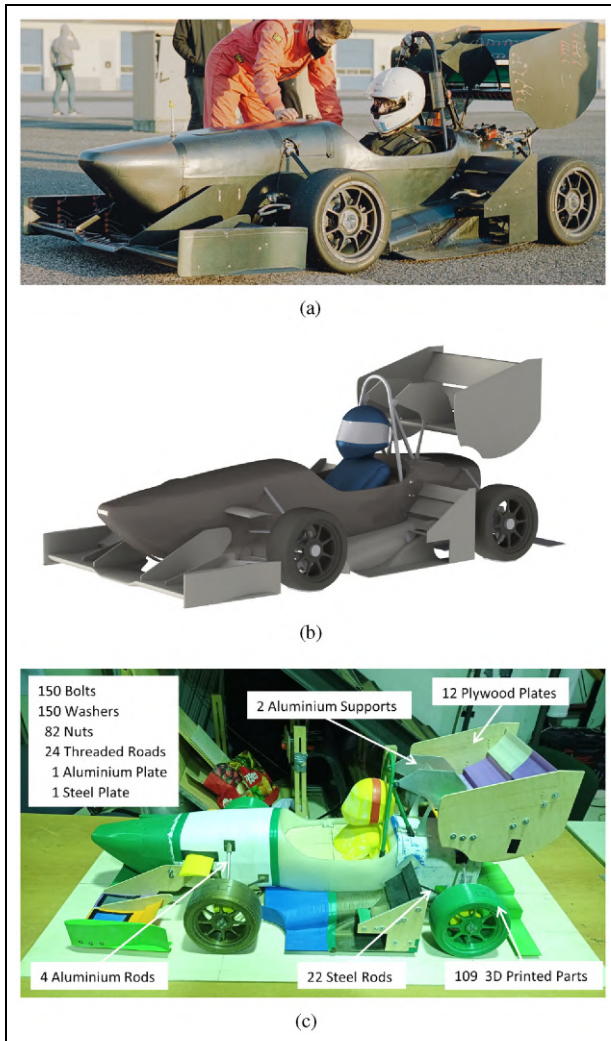


**Figure 15.** FST10e prototype: (a) full size vehicle, (b) render of WT model, and (c) WT model.

different Reynolds number that was also replicated in the CFD simulations.

The car model, ground plate, and force balance placement in the test chamber is shown in Figure 16.

## Experimental setup

### Test configurations

The effects of ground clearance are complex, because beneficial changes in one component can lead to detrimental to others, with uncertain overall outcome. This has been demonstrated for the case of formula racing cars with wide-span wings, such as the FST10e, where decreasing the clearance of the front wing had minor impact on its downforce but decreased significantly the front wheel lift due to the changed vortex paths.<sup>31</sup>

As such, to assess the effect of ground clearance on the FST10e aerodynamics, the model was tested at three different ground clearance configurations ( $RH1$ ,  $RH2$ , and  $RH3$ ) described in Table 3. The front and

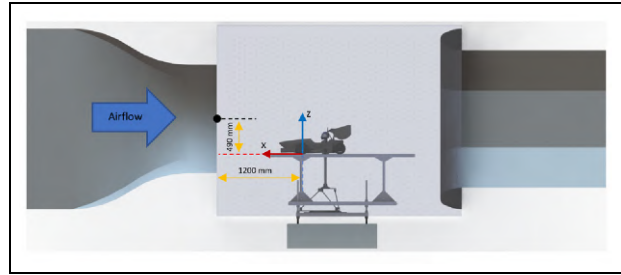


**Figure 16.** Model position inside the test chamber.

**Table 3.** Experimental ride heights.

Configuration	$RH1$	$RH2$	$RH3$
Front RH (mm)	10.5	15.4	20.0
Rear RH (mm)	21.5	28.7	35.6
Pitching angle ( $^{\circ}$ )	1.23	1.49	1.75

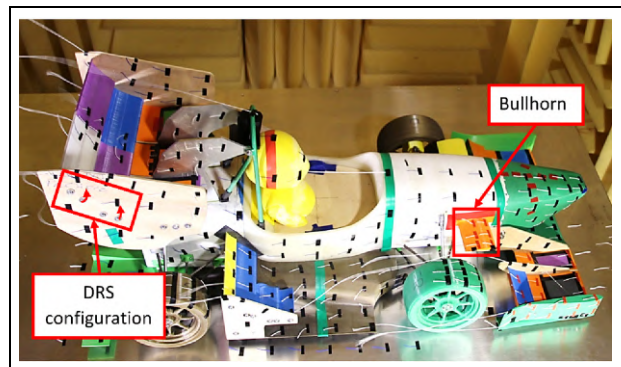


**Figure 17.** Configuration variation setups.

rear ride heights (RH) are the ground clearance of the monocoque plane at each car axle.

The first configuration was tested with ( $RH1$ ) and without bullhorns ( $RH1 - NB$ ), which are the short winglets located on the car nose aimed at generating vortices to control the downstream flow. The third configuration was experimented with two distinct rear wing setups, which were developed for different Formula Student dynamic events: the standard high downforce setup for the endurance event ( $RH3$ ) and the low drag setup recreating a Drag Reduction System (DRS) for the acceleration event ( $RH3 - DRS$ ). Figure 17 illustrates the changing components between configurations.

### Experimental procedure

The experimental tests required a vast number of systems (e.g. wind tunnel motor, force balance acquisition system, and temperature sensor) to work synchronously without any automated link among them.

During the experiments, the balance loads, WT temperature, and ground clearance were continuously monitored and recorded. The air temperature was kept at 27°C to match the WT characterization experiment. For safety reasons, the wind tunnel motor speed was increased in three steps, 15, 20, and finally 25 m/s. In every WT test run, two video cameras monitored the wheels displacement to ensure that no load was transferred from the car model to the ground plate. Finally, another camera was pointed at the nose of the car to measure the vertical displacement to monitor the pitch rotation of the car with increasing airspeed.

## Flow visualization

Before seeking for the correlation of the integral aerodynamic coefficients measured with the force balance and estimated with CFD, a detailed flow visualization was done to capture the performance of individual components on some critical parts, namely front wing, front wheel and bullhorn, lateral diffuser, rear wing, and rear diffuser.

Wool tufts were used as the visualization technique to provide diagnostic information relative to the airflow around the model. Despite being cheap and simple, they give a clear insight of the regions of cross-flow, reverse flow, and flow separation on the surfaces where they are attached to, as they point into the direction of the airflow near the surface.<sup>32</sup> It should be kept in mind that phenomena smaller than the tufts length might not have been captured, since they filter high frequency perturbations, and that the numerical simulations were time-averaged. Moreover, unsteady phenomena observed in videos were discussed but impossible to represent in images.

The following sections present a comparison between the tufts and the surface streamlines simulated numerically. The  $x$ -axis skin friction on the model surface is presented in two distinct colors: red ( $C_{f_x} > 0$ ) represents the attached airflow and blue ( $C_{f_x} < 0$ ) the separated airflow regions.

### Front wing

The front wing presented some major discrepancies between the experimental and numerical results. While the tufts captured some vorticity only near the trailing edge of the endplate (region 2 in Figure 18(a)) in the WT experiments, the numerical simulations estimated a large separation zone near the leading edge of the main plane (region 1 in Figure 18(b)).

The tufts located on the ground plate, in front of the wing, showed some motion, which means that the ground boundary layer had already become turbulent, so less prone to separation. That transition could have been induced by the supporting apparatus of the ground plate that affected the incoming airflow. To test this hypothesis, the CFD was repeated without a

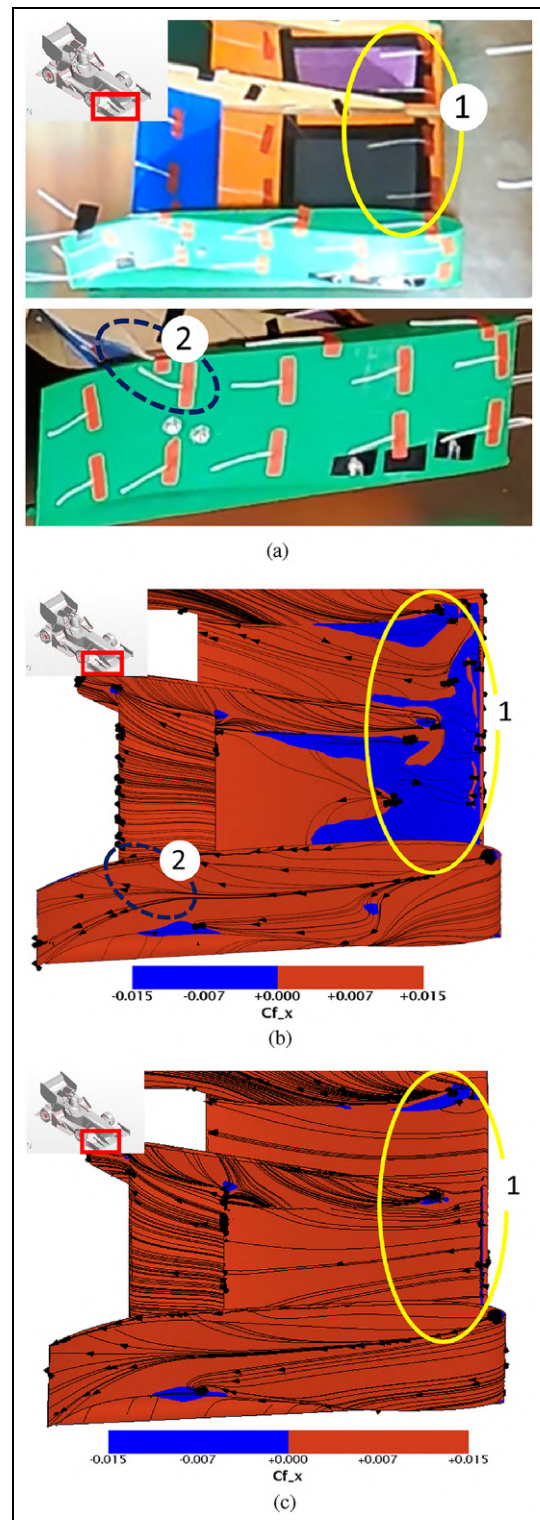


**Figure 18.** Front wing pressure side flow visualization (RH1): (a) experimental, (b) numerical with  $\gamma$  transition model, and (c) numerical without transition model.

transition model, thus assuming a fully turbulent flow reaching the front wing. Figure 18(c) shows that no separation on the front wing pressure surface is estimated, in much better agreement with the WT experiment. Therefore, the  $\gamma$  transition model did not recreate the physics observed inside the wind tunnel.

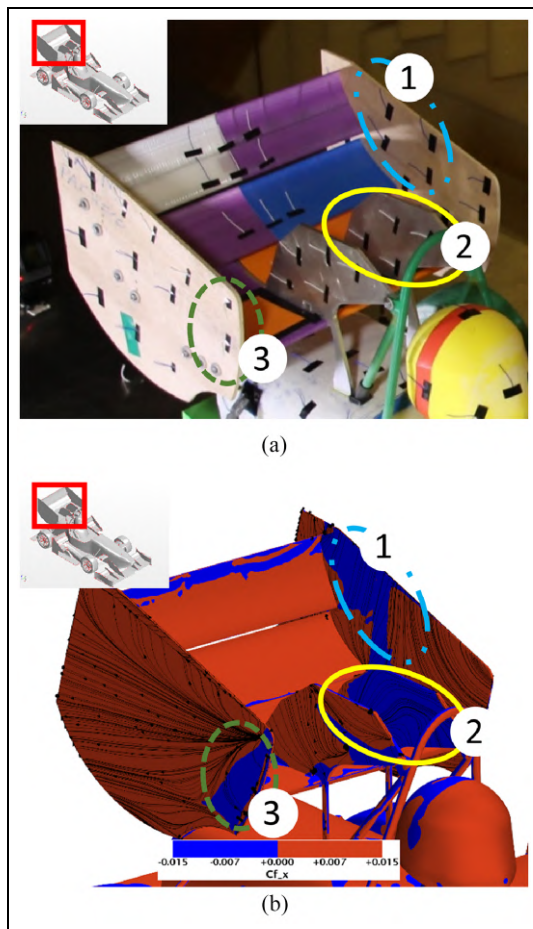


**Figure 19.** Rear wing flow visualization (RH1): (a) experimental and (b) numerical.

Regarding the endplate, the surface streamlines reproduced very well the wool tufts behavior in both simulations. Indeed, an upwash stream was noticed (region 2) corresponding to the upwash created by the front wing flap.

### Wheel and bullhorn

Two high turbulence regions were detected in the experiments: inboard of the bullhorn and on the tire upper region. The  $\gamma$  transition model proved to overestimated the separated region on both surfaces mentioned. As concluded in the Front Wing study, removing the transition model in the CFD proved again beneficial to recreate the tufts behavior.

### Rear wing

Similarly to the front wing, the rear wing also presented some differences between numerical and experimental tests, as illustrated in Figure 19.

The numerical simulations, shown in Figure 19(b), captured three large separation zones: endplate interior (region 1), rear wing supports interior (region 2), and endplate exterior (region 3). However, the tufts in the

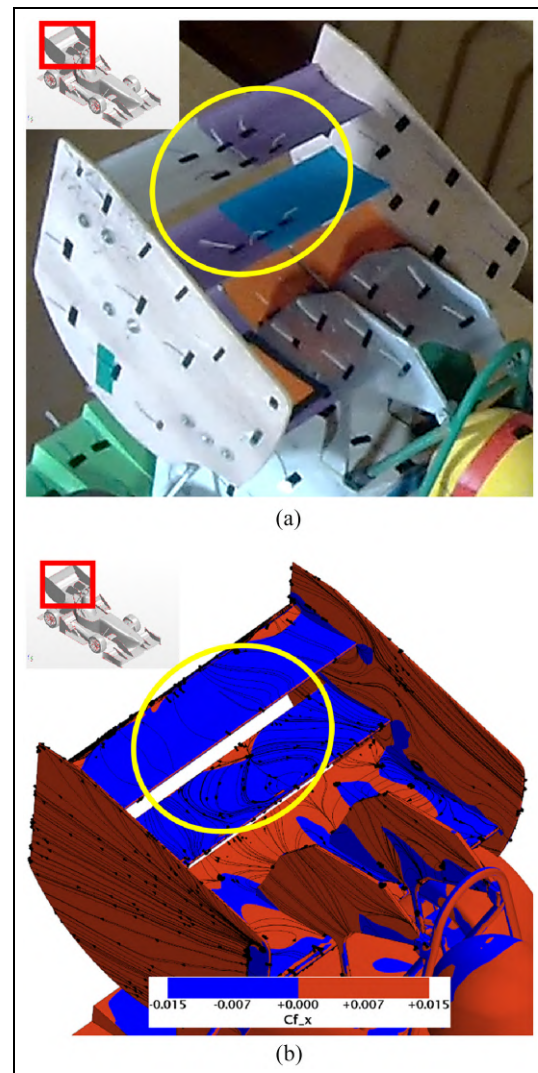


**Figure 20.** Rear wing flow visualization (RH3 – DRS): (a) experimental and (b) numerical.

experiments only showed a separation near the endplate leading edge as seen in region 3 in Figure 19(a). Not only does the air that reach the rear wing have very high turbulence intensity but also the wing geometry itself generates a complex airflow with combined longitudinal and transverse flow separation. This makes regions 1 and 2 extremely difficult to analyze using tufts.

Despite the airflow around the endplates being equally complex, affected by strong vortices, the numerical streamlines reproduced the tufts behavior on the outer endplate surfaces (region 3).

In the low drag RH3 – DRS configuration, both rear wing flaps were set at a slightly negative angle-of-attack, which caused separation on their pressure side by changing the stagnation points to the flaps suction side, as seen in Figure 20(b), in the numerical simulation. The tufts located on the flaps pressure side highlighted a high turbulence region, marked in Figure 20(a).

This rear wing configuration causes the pressure difference between the inner and outer part of the endplate

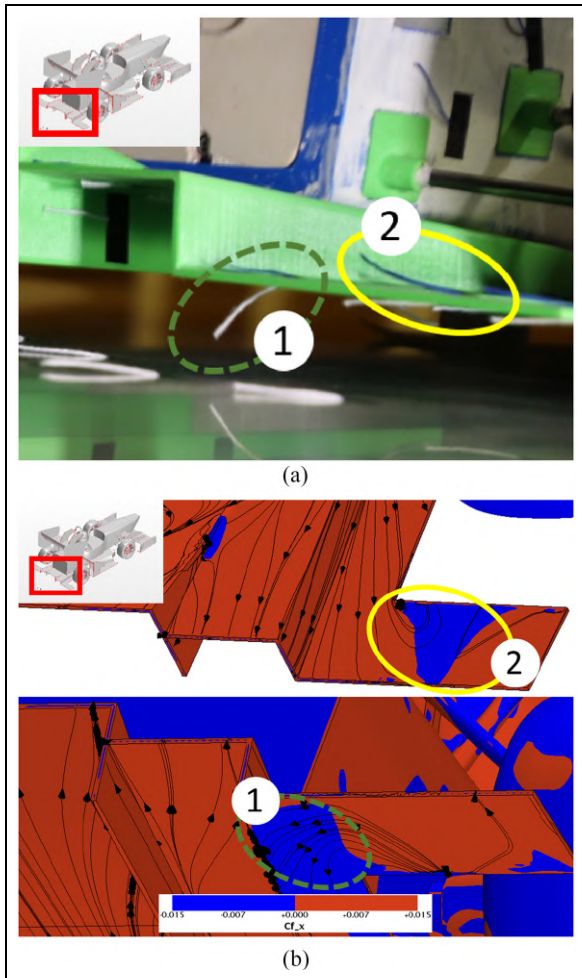


**Figure 21.** Rear diffuser flow visualization (RH1): (a) experimental and (b) numerical.

to be lower than in the no-DRS case, yielding a weaker endplate top vortex. The difference in the tufts behavior highlighted that change as well and, once again, the simulation streamlines matched that behavior.

**Underbody**

The FST10e underbody is composed by the rear diffuser and the lateral diffusers, as seen in Figure 1.

The downforce generated by the rear diffuser depends on the ride height, diffuser ramp angle, and its relative length to that of the vehicle length. It has been shown that different ride heights correspond to different diffuser ramp angles to achieve optimum downforce and aerodynamic efficiency,<sup>33</sup> which was taken into consideration by the FST design team.

The rear diffuser was the only component of the model underbody that could be visualized by placing a camera attached to the ground behind to visualize the tufts inside.

Although the tufts remained attached to the diffuser interior surfaces, proving its design, two separation zones outside were found (regions 1 and 2 in Figure 21(a)). These zones are on the diffuser flat plates located behind the wheel, whose aim is to prevent the wheel wake to enter the low pressure diffuser channel. Due to severe turbulence, it was not possible to conclude exactly what caused the registered tufts 3D motion.

For this part of the vehicle, the numerical simulation correlates very well with the experiments as attested in Figure 21(b).

**Aerodynamic loads**

Being the present work focused on the qualitative comparison between experimental and computational fluid dynamics, the quality of the numerical simulations was assessed by the captured trends in the nondimensional aerodynamic coefficients. Nevertheless, the quantitative results plotted include the associated uncertainty bars, where: the experimental uncertainty was estimated through the standard deviation of the data acquired in three runs repeated under the same conditions, which were effected by the car model apparatus, instrumentation, and WT facility; and the numerical uncertainty was estimated using the method already described. The results were normalized with the first value to allow an easier reading of the sensitivity evaluation.

**Ride height study**

This study evaluated the sensitivity of the model aerodynamics loads with the ground clearance of the

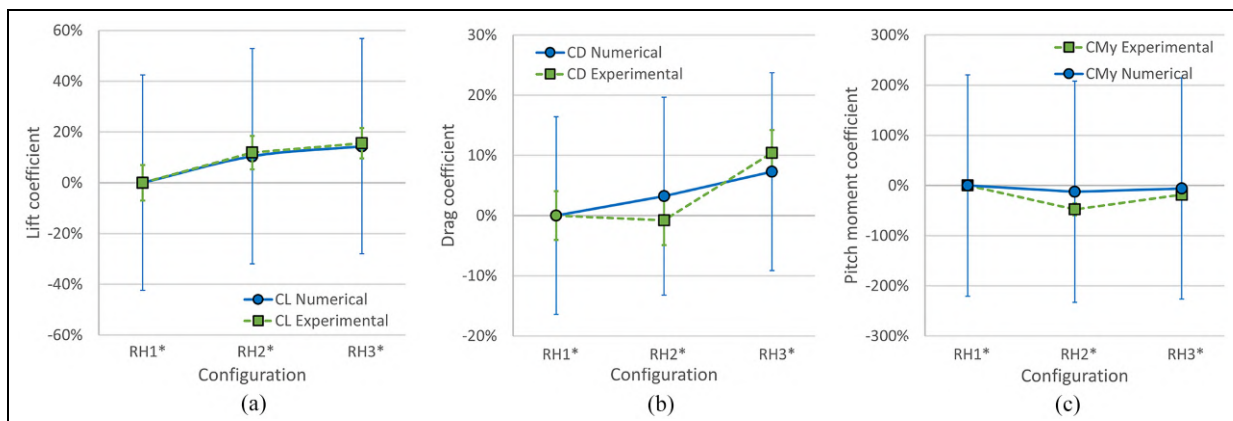


**Figure 22.** Ride height study aerodynamic loads: (a) downforce coefficient, (b) drag coefficient, and (c) pitching moment coefficient.

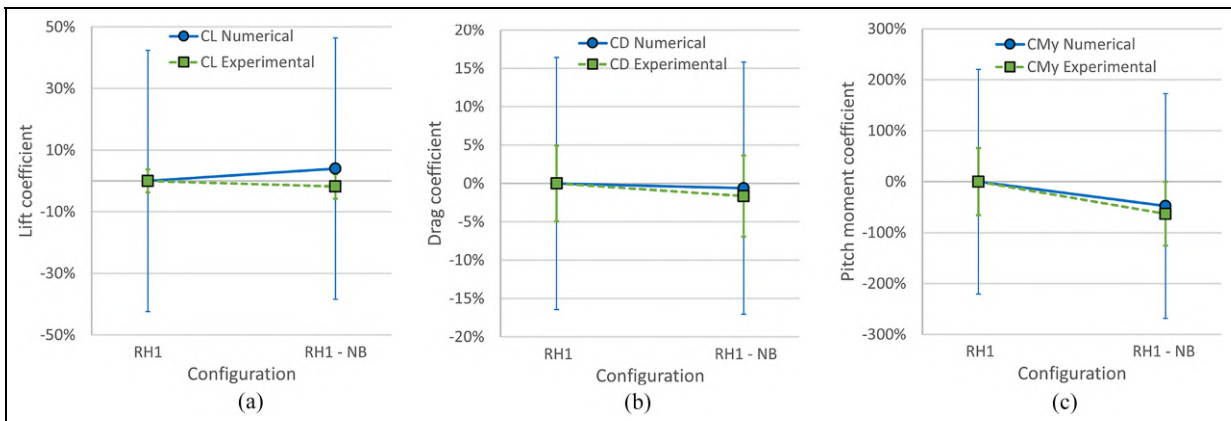


**Figure 23.** Bullhorn study aerodynamic loads: (a) downforce coefficient, (b) drag coefficient, and (c) pitching moment coefficient.

vehicle. Figure 22 reveals how the downforce, drag, and pitching moment coefficients behave with the different ride height settings listed in Table 3.

The experimental tests concluded that the downforce coefficient increases with the ground clearance, as seen in Figure 22(a). The increase in pitching angle, yielding both a steeper angle-of-attack of the wings and a stronger diffuser expansion, is the likely cause of such behavior. The numerical simulations captured the trend and sensitivity of the downforce of the experiments, which can be noted by having the same variation between the car configurations. The downforce coefficient exhibits higher sensitivity to lower ride heights, as the variation of 11% between *RH1* and *RH2* configurations and 3.25% between *RH2* and *RH3* demonstrate.

As expected, the drag coefficient, shown in Figure 22(b), also followed the increasing behavior of the downforce coefficient, as a consequence of increased induced drag. During the experimental tests, the *RH2* configuration presented a slight decrease in drag while the pitching moment increased, which the numerical simulation could not estimate. However, the numerical simulations captured the same behavior of the experimental drag coefficient for the *RH1* and *RH3* configurations.

The variations in the pitching moment coefficient registered experimentally were not properly captured by the numerical simulations, as seen in Figure 22(c). The experimental tests presented an initial increase with increased ride height, from *RH1* to *RH2*. This resulted from the unexpected slight decrease in drag combined with an increase in downforce which, given that the reference point for the moment sits below and fore of the center of pressure, led to an increased nose up moment contribution. Moreover, the trends of the pitching moment coefficient are also affected by the center of pressure, which changes continuously through the different right height configurations and cannot be neglected. However, looking at the ride height extreme settings tested, configurations *RH1* and *RH3*, both experimental and numerical correlate well in indicating an almost null sensitivity of pitching moment. This

means that the car aerodynamic balance is not much effected by the ride height and it can be adjusted primarily by the front and rear wing flaps incidence angle.

### Bullhorn study

Despite generating lift, the bullhorns are meant to improve the airflow around the car by reducing the upwash generated by the front wing and redirecting the airflow to the side and rear wings, shifting the center of pressure (CoP) rearwards. At the same time, they create a vortex to control the wheel wake and push away the air with energetic losses, located on the side of the car. Furthermore, they also counter the vortex generated by the rear wing endplate by rotating in the opposite direction, reducing the overall induced drag. Since the bullhorn performance is directly dependent on the vortices effectiveness, its position can be hard to establish from numerical simulations due to the difficulties to avoid excessive diffusion at the vortex core.

The first ride height configuration was tested with (*RH1*) and without bullhorns (*RH1 - NB*), leading to the comparison between the numerical and experimental results presented in Figure 23.

The downforce coefficient, shown in Figure 23(a), exhibits a small variation but with contrasting behavior depending on the analysis. While the WT experiments show a slight increase with bullhorns (*RH1 - NB*), the CFD capture an opposite trend.

The drag and pitching moment coefficients, shown in Figure 23(b) and (c) respectively, present the same trend in both experimental tests and numerical simulations, with almost matched sensitivity. Both methods agree in estimating a slight increase of drag and decrease of pitching moment due to the bullhorns.

Analyzing the pitching moment, it is clear that there is a fair correlation between the methods in terms of sensitivity, despite the differences in absolute values. It was verified that the bullhorns cause a rearwards shift of the CoP. Without bullhorns, the CoP present higher sensitivity in the numerical simulations, where it shifts

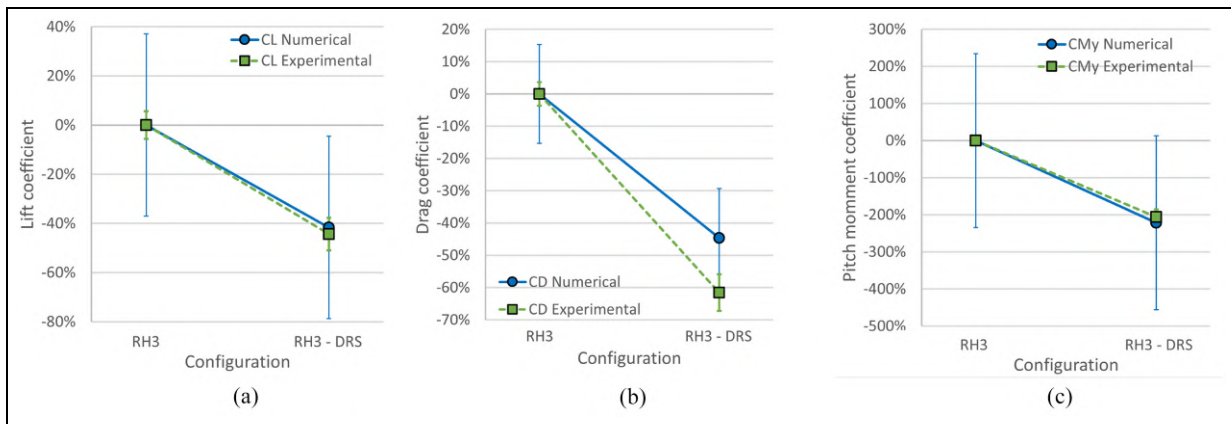


**Figure 24.** DRS study aerodynamic loads: (a) downforce coefficient, (b) drag coefficient, and (c) pitching moment coefficient.

forward approximately 7.4% in contrast with 2.8% in the experimental tests.

Both the experiments and the simulations indicate that the current bullhorn design is not effective, leading to a decrease in downforce and an increase in drag. In addition, the bullhorns also shift the CoP rearwards, which has a negative impact on the car handling since the FST10e car has already the CoP located behind the center of gravity.

### DRS study

A low drag configuration is desired for the acceleration event in the FS competition. This is achieved by decreasing the incidence angle of the two flaps after the main rear wing element, as illustrated in Figure 20, at the expense of reduced downforce. To assess the impact of such setting, the car model was tested for the upper and lower limits of the rear wing flaps incidence adjustment range, corresponding to configurations *RH3* and *RH3 - DRS*, respectively, being the results illustrated in Figure 24.

The numerical simulations very accurately capture the same trends as those experimentally measured for the three aerodynamic coefficients studied. As expected, both the downforce and drag coefficients decrease significantly in the low drag *RH3 - DRS* configuration, as shown in Figure 24(a) and (b), respectively.

The sensitivity of the downforce coefficient to DRS is accurately captured by CFD, despite the existence of a significant offset in the absolute value. Between the high-drag configuration (*RH3*) and the low-drag configuration (*RH3 - DRS*), the wind tunnel downforce coefficient presents a decrease of  $-44.3\%$ , which is slightly higher comparing with the decrease of  $-41.7\%$  for the numerical downforce coefficient, as shown in Figure 24(a).

Regarding the drag coefficient, shown in Figure 24(b), the wind tunnel drag coefficient present a decrease of  $-61.6\%$  between the high-drag configuration (*RH3*) and the low-drag configuration (*RH3 - DRS*). Interestingly, the numerical simulation

does not estimate a sensitivity of the drag coefficient as high as that obtained in the experimental tests, which decreased only  $-44.6\%$ , meaning that the CFD fails to fully capture the overall drag reduction.

Nonetheless, the differences between experiments and simulations are smaller than the estimated uncertainties.

As for the pitching moment coefficient, the occurrence of a strong shift of the CoP between the high-drag and low-drag configurations is highlighted in Figure 24(c). During the experimental tests, the CoP of the configuration *RH3* was located rearwards from the attachment point (nose down  $C_M < 0$ ) and shifted forward with the *RH3 - DRS* configuration (nose up  $C_M > 0$ ). The numerical simulation was able to very accurately capture not only the same behavior of the experiments but also replicate the absolute values.

The strong effect of deploying the DRS system on the car aerodynamic balance must be carefully managed by the pilot, since the car behavior can dramatically change from understeering to oversteering. The shift in pitching moment was corroborated by the registered motion of the car model during the wind tunnel experiments, as documented in Figure 25.

### Conclusions

The main goal of this work was to test a complete Formula Student vehicle model in a wind tunnel to validate the numerical simulations used in its aerodynamic design process.

The numerical simulations were based on an automated parametric CAD model which enabled a quick generation of the entire CFD model that replicated the WT conditions and car setup. A medium-refinement mesh level with 13.7 million cells was used that provided simulations in about 17.5h with relatively low errors, 5.8% for the downforce coefficient and 4.3% for the drag coefficient.

The one-third scale, 3D printed, FST10e formula student model replicated the prototype geometry in

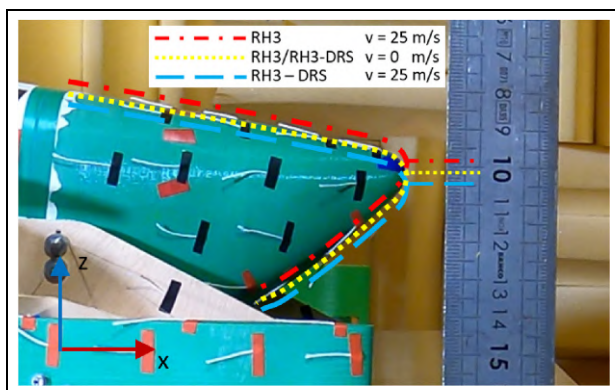


**Figure 25.** RH3-DRS configuration pitch rotation.

much detail, while being sturdy and easy to adapt to new aerodynamic parts to be tested in the future.

The flow visualization technique using the wool tufts revealed to be simple, low-cost, yet effective. It enabled a quick identification of flow separation and turbulence zones, such as the identification of fully turbulent flow impinging the front wing, which caused the transition model to be dropped in CFD to get a better match with the WT airflow. Overall, a very good correlation between the tufts orientation in the WT experiments and the streamlines in the numerical simulations was obtained. As expected, complex flow structures obtained from numerical simulations could not be replicated with tufts, such regions of 3D cross-flow or strong and/or high-frequency unsteadiness.

The results clearly demonstrated a strong correlation between the WT experimental data and the CFD simulations in terms of integral aerodynamic coefficients in most cases studied. Even though the associated estimated uncertainties did not enable a full quantitative evaluation of the aerodynamic performance, not only the sensitivity to certain parameters was accurately captured but also the performance parameters showed a very good quantitative agreement under some conditions. Among the three parameters studied, the DRS device was the one that had the greatest impact on the aerodynamic coefficients, as expected, thus the correlation between WT and CFD was also the strongest. Remarkably, even though the other two parameters – ride height and bullhorns – produced a much weaker impact, an overall good correlation was still demonstrated.

This extensive work provides evidence that the CFD setup used in studies by the FST Lisboa aerodynamic design team correlates well with WT testing, building confidence that trends estimated in numerical parametric studies are likely to be translated to the real prototype performance.


#### Declaration of conflicting interests

The author(s) declared no potential conflicts of interest with respect to the research, authorship, and/or publication of this article.

#### Funding

The author(s) disclosed receipt of the following financial support for the research, authorship, and/or publication of this article: This work was supported by FCT, through IDMEC, under LAETA, project UIDB/50022/2020.

#### ORCID iD

André C Marta  <https://orcid.org/0000-0002-9399-7967>

#### References

- Katz J. *Race car aerodynamics: designing for speed*. 2nd ed. Cambridge, MA: Bentley Publishers, 1996.
- Tu J, Yeoh GH and Liu C. *Computational fluid dynamics: a practical approach*. 3rd ed. Amsterdam: Butterworth-Heinemann, 2018.
- Fu C, Bounds CP, Selent C, et al. Turbulence modeling effects on the aerodynamic characterizations of a NASCAR Generation 6 racecar subject to yaw and pitch changes. *Proc IMechE, Part D: J Automobile Engineering* 2019; 233(14): 3600–3620.
- Knowles RD, Saddington AJ and Knowles K. On the near wake of a Formula One front wheel. *Proc IMechE, Part D: J Automobile Engineering* 2013; 227(11): 1491–1502.
- Institution of Mechanical Engineers. Formula Student, <https://www.imeche.org/events/formula-student> (2022, accessed 5 October 2022).
- Formula Student Germany. FS rules 2021, <https://www.formulastudent.de/fsg/rules> (2020, accessed 5 October 2022).
- Hatton G. Tech explained: formula Student aerodynamics. *Racecar Engineering*, <https://www.racecar-engineering.com/articles/tech-explained-formula-student-aerodynamics> (2017, accessed 12 October 2022).
- Rembold B. 3D flow measurement in the wind tunnel—a Formula Student case study. *AirShaper*, <https://airshaper.com/blog/3d-flow-measurement-formula-student> (2020, accessed 12 October 2022).
- Gilles T, Routly J, Sheffer C, et al. Wind tunnel model and control system. *Design Show 6 University of Southampton*, <https://uosdesign.org/designshow2020/project/wind-tunnel-model-and-control-system/> (2020, accessed 12 October 2022).
- Barlow JB, Rae WH and Pope A. *Low speed wind tunnel testing*. New York, NY: Wiley, 1999.
- Farrell TE and Miller LS. Development of a new boundary layer control technique for automotive wind tunnel testing. In: *44th AIAA aerospace sciences meeting and exhibit*, Reno, NV, USA, 9–12 January 2006.
- Hennig A, Widdecke N, Kuthada T, et al. Numerical comparison of rolling road systems. *SAE Int J Engines* 2011; 4(2): 2659–2670.
- Fago B, Lindner H and Mahrenholtz O. The effect of ground simulation on the flow around vehicles in wind tunnel testing. *J Wind Eng Ind Aerodynamics* 1991; 38: 47–57.
- Hucho WH. *Aerodynamics of road vehicles*. London: Butterworth-Heinemann Ltd, 1987.
- Bauman RP and Schwaneberg R. Interpretation of Bernoulli's equation. *Phys Teach* 1994; 32(8): 478–488.



16. de Brederode V. *Aerodinmica incompressvel: fundamentos*. 1st ed. Lisboa: IST Press, 2014.
17. Spalart PR and Rumsey CL. Effective inflow conditions for turbulence models in aerodynamic calculations. *AIAA J* 2007; 45(10): 2544–2553.
18. Oliveira A. *Design, construction, calibration and testing of a wind tunnel force balance*. Master's Thesis, Instituto Superior Técnico, Portugal, 2020.
19. Gonzalez M, Ezquerro JM, Lapuerta V, et al. Chapter 7. Components of a wind tunnel balance: design and calibration. In: JC Lerner and U Boldes (eds) *Wind tunnels and experimental fluid dynamics research*. Rijeka: IntechOpen, 2011, pp.115–134.
20. Reynolds O. On the dynamical theory of incompressible viscous fluids and the determination of the criterion. *Proc R Soc Lond A Math Phys Sci* 1995; 451(1941): 5–47.
21. Menter FR. Two-equation eddy-viscosity turbulence models for engineering applications. *AIAA J* 1994; 32(8): 1598–1605.
22. Bounds CP, Zhang C and Uddin M. Improved CFD prediction of flows past simplified and real-life automotive bodies using modified turbulence model closure coefficients. *Proc IMechE, Part D: J Automobile Engineering* 2020; 234(10–11): 2522–2545.
23. Zheng X, Liu C, Liu F, et al. Turbulent transition simulation using the  $k-\omega$  model. *Int J Numer Methods Eng* 1998; 42(5): 907–926.
24. Sosnowski M, Krzywanski J, Grabowska K, et al. Polyhedral meshing in numerical analysis of conjugate heat transfer. *EPJ Web Conf* 2018; 180: 02096.
25. Vallikivi M, Hultmark M and Smits AJ. Turbulent boundary layer statistics at very high Reynolds number. *J Fluid Mech* 2015; 779: 371–389.
26. Ea L. *Aerodinmica incompressvel: exceccios*. 1st ed. Lisboa: IST Press, 2015.
27. Mou SC, Luan YX, Ji WT, et al. An example for the effect of round-off errors on numerical heat transfer. *Numer Heat Transf B Fundam* 2017; 72(1): 21–32.
28. Tu J, Yeoh GH and Liu C. Chapter 6. CFD solution analysis: essentials. In: J Tu, GH Yeoh and C Liu (eds) *Computational fluid dynamics*. 3rd ed. Amsterdam: Butterworth-Heinemann, 2018, pp.211–253.
29. Eça L, Vaz G, Toxopeus SL, et al. Numerical errors in unsteady flow simulations. *J Verification Validation Uncertain Quantif* 2019; 4(2): 021001.
30. Eça L and Hoekstra M. A procedure for the estimation of the numerical uncertainty of CFD calculations based on grid refinement studies. *J Comput Phys* 2014; 262: 104–130.
31. Diasinos S, Barber T and Doig G. Numerical analysis of the effect of the change in the ride height on the aerodynamic front wing–wheel interactions of a racing car. *Proc IMechE, Part D: J Automobile Engineering* 2017; 231(7): 900–914.
32. JP. Crowder Chapter 9. Tufts. In: WJ Yang (ed.) *Handbook of flow visualization*. New York, NY: Routledge, 2001, pp.131–180.
33. Knight J, Spicak M, Kuzenko A, et al. Investigation of vehicle ride height and diffuser ramp angle on downforce and efficiency. *Proc IMechE, Part D: J Automobile Engineering* 2019; 233(8): 2139–2145.